Thermoelastic effects in Bragg reflectors as a potential bottleneck for XFELs with megahertz repetition rate
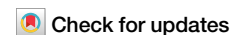
Check for updates

Immo Bahns [1] ✉, Patrick Rauer [2], Jörg Rossbach [3], Sebastian Steinlechner [4,5] & Harald Sinn[1]

Bragg reflectors are essential for beam transport in X-ray free-electron laser (XFEL) facilities. On interaction with Bragg reflectors, a part of the pulse energy will be absorbed, causing the propagation of displacement waves due to rapid thermal expansion. It is suspected that these waves may cause stability problems for XFELs operating with megahertz repetition rates. Here, we experimentally investigate the displacement of a diamond Bragg reflector induced by an optical ultra-violet laser pulse, simulating XFEL pulses with mJ pulse energy, both at room temperature and cryogenic temperatures. Our experiment shows negligible damping of the displacement waves on µs timescales, which could cause disruption for subsequent XFEL pulses. We compare our measurements to a simulation framework based on the assumptions of local thermodynamic equilibrium and classical mechanics, observing reasonable agreement. Our results show that thermoelastic effects are critical for a reliable stability assessment of Bragg reflectors, but are often overlooked.

In addressing the fundamental question of the impact of high repetition rates in modern X-ray free-electron laser (XFEL) facilities on Bragg reflectors, our experiments provide crucial insights that clarify uncertainties in classical thermoelastic models, particularly under low-temperature conditions, where simulative predictions may be less reliable. In modern X-ray free-electron laser (XFEL) facilities, such as the European XFEL[1], the Linac Coherent Light Source-II (LCLS-II) upgrade[2] or the Shanghai High repetition rate XFEL and Extreme Light Facility (SHINE)[3], photon pulse energies in the mJ range with repetition rates in the megahertz range can be achieved. These photon pulses enable cutting-edge experiments in various research fields[4–7]. However, the high repetition rates also raise new challenges, like the risk of sample damage induced by shock waves in sample-carrying liquid jets[8]. Further, as has been theoretically predicted[9–14] and experimentally observed in operation at the European XFEL[12,13], the increased repetition rate of superconducting FELs increases the heat load for X-ray optics and causes changes in the diffraction condition with time. This can introduce stability issues for the actual operation. Established theoretical frameworks can be found in the literature to evaluate the stability of diffraction conditions by considering strain in the context of a dynamical X-ray diffraction theory[9–11,15–18]. In this work, we apply such a framework[15] to assess in detail which new stability issues may be faced by taking into account thermoelastic effects. Bragg reflectors with stable reflection conditions are essential for various X-ray optics devices at these XFEL facilities, like spectrometers[19–21], self-seeding setups[13,22] and future advanced X-ray cavity-based installations such as cavity-based X-ray free-electron lasers (CBXFEL)[23–27] and X-ray laser oscillators (XLO)[28]. A common choice for a Bragg reflector in modern XFEL facilities is a single crystalline diamond because of its radiation hardness and outstanding stability under heat load[29]. The heat load is attributed to the interaction between photons and matter, which involves the absorption of energy and its subsequent conversion into heat. The pulse duration of an XFEL photon pulse is typically in the range of a few tens of femtoseconds. However, the exact pulse length can be considered of minor importance in the context of a thermoelastic simulation framework, as the thermalization time after absorption of the photon pulse energy is expected to be on the picosecond scale[30]. The rapid thermal expansion on the picosecond time range, induced by the absorption of pulsed electromagnetic waves, was investigated experimentally by several authors at room temperature[31–33]. Also, calculations based on the theory framework of thermoelasticity[34] were carried out analytically for the one-dimensional case and numerically for the three-dimensional axisymmetric case to predict strain wave propagation[14,35–37]. In our recently published article on thermoelastic simulations[14], it was suspected that thermoelastic

[1]European XFEL, Holzkoppel 4, 22869 Schenefeld, Germany. [2]Deutsches Elektronen-Synchrotron DESY, Notkestr. 85, 22607 Hamburg, Germany. [3]Universität Hamburg, Institut für Experimentalphysik, Luruper Chaussee 149, 22761 Hamburg, Germany. [4]Department of Gravitational Waves and Fundamental Physics, Maastricht University, P.O. Box 616, 6200 MD Maastricht, The Netherlands. [5]Nikhef, Science Park 105, 1098 XG Amsterdam, The Netherlands. ✉e-mail: immo.bahns@xfel.eu

effects can be limiting for the stability of cryogenically cooled diamonds for CBXFEL applications. However, the theoretical framework of thermoelasticity is based on classical physics approaches given by continuum mechanics and the empirical Fourier heat law to describe heat transfer. Under the assumption of a local thermodynamical equilibrium, the Fourier heat law can be used to model the solid state heat transfer by quantized lattice excitations, the phonons[38]. However, the assumption of a local thermodynamic equilibrium is based on time and length scales of interest much larger than the mean free path and mean scattering time of the phonons. These conditions are typically not met for diamond Bragg reflectors at low temperatures[14]. To our best knowledge there is no experimental study available yet assessing the validity of the classical thermoelastic model at low temperatures. Therefore, we developed an experimental setup to probe the three-dimensional thermoelastic response under realistic heat load conditions for a cryocooled diamond crystal. The heat source used in our experimental setup is given by the absorption of an optical UV laser pulse, which generates a heat load comparable to that expected from a saturated XFELO pulse. To get insights into the temporal development of the strain field in the diamond crystal, we measured the surface displacement with an interferometer. The data from the interferometer measurement was then compared to numerical thermoelastic simulations based on the classic approximations. We present our findings considering an initial crystal temperature of 300 K, where the assumptions of local thermodynamic equilibrium are reasonable. This allows us to assess both the validity of the experimental approach and the general reliability of our simulation. Additionally, we investigate a condition with an initial temperature of 60 K, achieved through cryogenic cooling, to further evaluate the regime where the assumptions of the Fourier heat are not met. Comparison of our measurements and simulations indicate reasonable predictions of wave propagation for initial temperature values of 300 K as well as for 60 K. Nevertheless, at cryogenic temperature slight deviations, which cannot be explained by our error calculations, indeed give hint that a failure of the Fourier heat law was observed. Further, our interferometer-based measurements revealed that on timescales in the range of 100 μs the amplitudes of the displacement show no significant damping effects. This indicates that the displacement fields created by successive X-ray pulses with a megahertz repetition rate will interact with each other. Overall, our experimental findings emphasize the relevance of thermoelastic stability problems for saturated CBXFELs.

Results

Displacement measurement at the surface of a diamond crystal induced by a pulsed UV laser

Our experimental configuration (Fig. 1) may be referred to as a pump-probe measurement, in which the UV pulse is the pump generating a heat load-induced displacement wave and the probe is the interferometric signal change of the CW laser intensity measured on the oscilloscope, which is connected to the surface displacement. The oscilloscope measurement is triggered by the UV laser (see Methods for details) as illustrated in Fig. 1a. Since the UV laser outputs very stable pulses with a duration of about 1 ns and a repetition rate of 20 Hz, the signal-to-noise ratio can be improved by measuring the average of multiple pump-probe sweeps.

In our measurement, the spatial dimensions of the heat load profile are defined by the circular spot size of the UV laser with a Gaussian beam profile and the penetration depth, which is a measure for the exponential decrease of UV laser intensity in the diamond Bragg reflector. To imitate the heat load generated by a powerful X-ray pulse, we used an optical UV laser with a pulse energy of (45 ± 5) μJ. The beam radii of the pump and the probe laser were measured with a knife-edge technique[39] at the position of the diamond crystal. These measurements revealed a radius of (300 ± 12) μm for the UV laser and (45 ± 3) μm for the CW laser. The investigated Bragg reflector is a single crystalline chemical vapor deposition (SC CVD) diamond, with a thickness of (100 ± 10) μm and lateral dimension as sketched in Fig. 2a. The penetration depth of the diamond at the pump laser wavelength of 213 nm is about 5 μm and the reflectance is about $R = 0.22128$[40]. In our simulations, it

is assumed that the value of the penetration depth and the reflectance are approximately constant values for the temperature range investigated in this paper (see Methods for details). Assuming that the entirety of the absorbed energy of the laser will be converted into heat energy, the total heat load is about 35 μJ per pulse. Considering the energy distribution of the absorbed pulse energy yields a heat load profile with a similar energy density profile as expected for a single saturated CBXFEL pulse[24]. The impact of heating connected to the weak absorption of the CW laser photons can be neglected in the context of our experiment.

The heat load-induced surface displacement is measured with a Michelson interferometer, which uses a CW laser with a wavelength of 532 nm. The investigated displacement amplitudes in this work are smaller than 2 nm. Therefore, the intensity changes around a stabilized working point of the interferometer, which is set between constructive and destructive interference, yields an approximately linear relation between the voltage signal, measured by the oscilloscope, and the displacement of the crystal surface. The ultrafast photodiode used in combination with a high-speed oscilloscope captures signals in a frequency range from 10 kHz to about 4 GHz with almost constant amplification. For the interferometric measurement, the CW laser was aligned in the center of the UV laser, but the reflection used for the displacement measurement takes place at the opposite crystal surface with respect to the surface which is first met by the UV laser (as illustrated in Fig. 2a, b).

To investigate the impact of the temperature-dependent material parameters of diamond on the heat load-induced displacement wave, cryogenic cooling was used in our experimental setup. The lower part of the diamond crystal (Fig. 2a) is clamped with a holder design shown in Fig. 1c–e. A cryogenic cooler (Fig. 1b) in combination with a heater (Fig. 1d) is used to adjust the initial crystal temperature. The initial temperature of the diamond is assumed to be directly connected to the values of the temperature measured with the PT100 resistors at the holder (Fig. 1e). The estimation of the tolerance for the initial temperature value is based on the temperature difference of the two PT100 resistor measurements. Two different initial temperature values of (300 ± 3) K and (60 ± 3) K are considered in this paper.

To evaluate the systematic errors caused by signal contributions not directly related to the interferometric signal, we carried out three different test-measurements. First, the CW laser was turned off to check the direct impact of the UV light on the measurement. This revealed that using a long-pass filter, the signal contribution of the UV laser could be damped below the noise level of the oscilloscope. In the second test measurement the UV laser was blocked such that no direct radiation reaches the crystal, while allowing a trigger signal to reach the oscilloscope. In this case a signal on the order of magnitude of the oscilloscope noise was measured, which demonstrates that no surrounding noise sources affect the measurement in a noticeable manner. In the third measurement, one interferometer arm was blocked as sketched in Fig. 3a. The signal measured this way could then be traced back to the change of the diamond's reflective index induced by the interaction with the UV-laser pulse. In Fig. 3b, c it can be seen that this effect has a noticeable amplitude, hence causing a significant systematical error of the interferometric measurement. Nevertheless, the signal given by the interferometric signal is, apart of a strong initial peak in the beginning of the measurement, the dominating signal contribution. Therefore, it is still a reasonable approximation to connect the interferometric measurement directly to the surface displacement, as has been done in Fig. 3d, e. Interestingly, the amplitude and sign of the strong peak at the beginning of the signal changes with the initial temperature. For the measurement shown in Fig. 3d, e the crystal together with the UV laser have been translated to a position such that the signal amplitude is maximized. As deduced from the simulation presented in the next section, the maximum displacement is measured when the centers of the CW laser and UV laser, which both have a Gaussian beam profile, overlap. Interestingly, we noted that misaligning the center positions by a few tens of μm can also change the sign and amplitude of the strong initial peak of the measured signal.

Characteristic for both measurements is that after a time span of a few hundred of nanoseconds a maximum amplitude is reached and afterwards
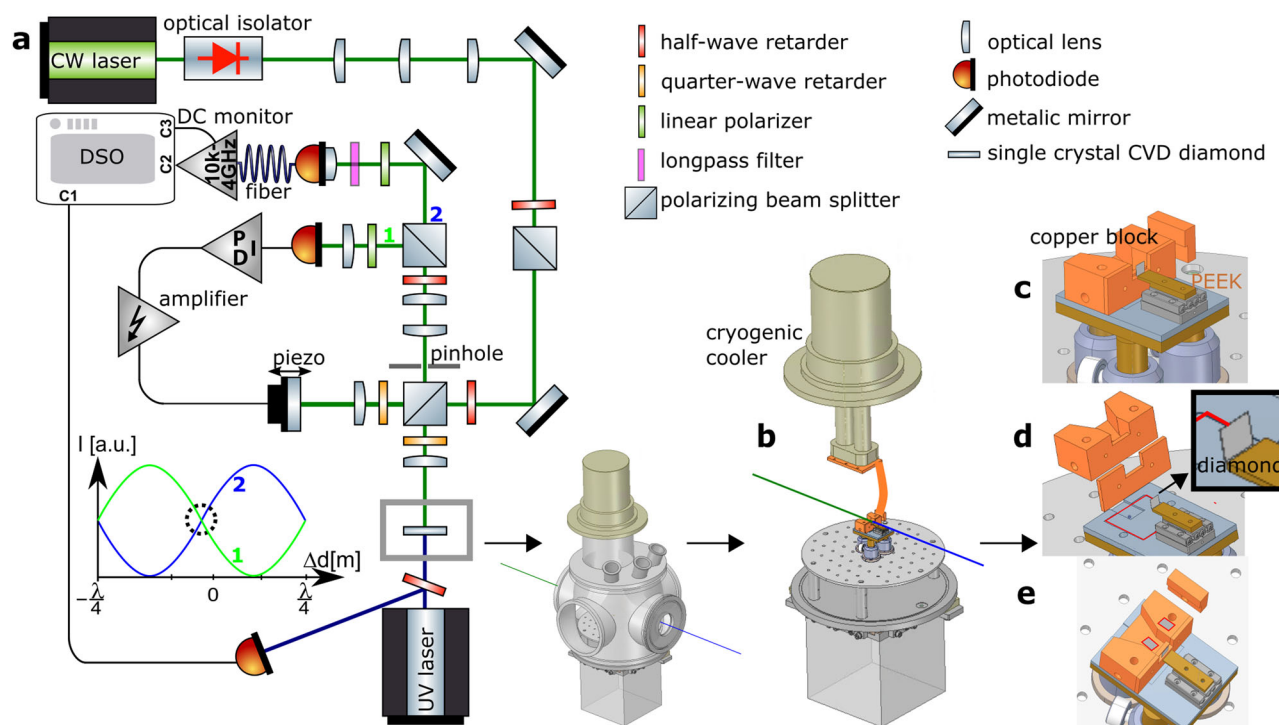
Fig. 1 | Experimental configuration for thermoelastic-induced displacement measurements in a diamond crystal. a Overview of experimental setup. An UV laser induces a heat load to a diamond crystal and also triggers the measurement captured by a digital storage oscilloscope (DSO). A Michelson-interferometer using a continuous wave (CW) laser measures the displacement, created by the heat load, at the rear side of the diamond crystal. An optical isolator is used to reduce back reflection into the laser. Polarizing beam splitters (PBS) in combination with half-wave retarders and linear polarizers are used to align the laser. Metallic mirrors give control over the beam path and optical lenses change the beam radius and divergence to the desired values. Quarter-wave retarders in combination with a half-wave retarder and a PBS are aligned such that the beams of the interferometer arms can interfere with each other. This gives two interferometer signals (green1 and blue2) with contrary response, as highlighted in the intensity function diagram. One signal (green1) is used to adjust the working point (marked with a dashed circle) between

constructive and destructive interference. The stabilization is ensured by a proportional–integral–derivative (PID) controller which aligns the position of a mirror mounted on a piezo-mover. The other signal (blue2) is used for a measurement with the DSO. An ultrafast photodiode is directly connected to the DSO using a multimode optical fiber signal, to measure signals in a frequency range of 10 kHz to 4 GHz. A DC monitor gives the ability to monitor the working point stabilization. A pinhole is used to block the undesired front side reflection from the wedged diamond crystal. An optical long pass filter blocks direct contribution of the UV laser light. **b** The diamond crystal is placed in a vacuum chamber. The holder is connected to a cryogenic cooler via a flexible copper strap. **c** A linear positioning stage with a polyether ether ketone (PEEK) block on top is used to clamp the diamond crystal. **d** A modified illustration of **c** marks the position of a Kapton heater (red marked), placed to adjust the holder/crystal temperature. **e** The temperature of the holder is measured with PT100 resistors at two different positions (red marked).

an oscillation without a simple periodic pattern takes place around the zero position. The damping of this oscillation seems to be too low to be directly visible on the timescales of 100μs. Measuring the damping factor of these oscillations has so far not been investigated with our current experimental setup. However, it can be concluded from the measurements for time <0 in Fig. 3d, that all oscillations, which are greater than the noise level of our experimental setup, are damped to a negligible value after a time span of 50 ms (repetition rate of the UV laser).

Simulations of the deformation field for a diamond Bragg reflector

For the numerical simulation (see Methods for details) the axisymmetric partial differential equations (PDEs) of thermoelasticity are solved by neglecting the coupling effect of the displacement field on the temperature field. The geometry used in the simulation is a cylindrical crystal with a radius of 2 mm. We derived the thickness from the longitudinal speed of sound and the time period, which is needed for a displacement wave to travel from the front to the rear side of the crystal. The propagation of such longitudinal waves is well understood[31–33]. It can be derived from that knowledge that the periodic fringes marked by light gray vertical lines in Fig. 4a, b correspond to the time period which is needed for the above-mentioned thickness calculation (details are explained in the Methods section).

The material parameters considered are the same as described in one of our previous publications[14]. To estimate the reliability of our simulations, the tolerances for the material parameters have been considered. Since the isotope concentration has a significant impact on the thermal conductivity[41] and it is not known exactly for our measurement, we chose a quite large tolerance of ±20% on the thermal conductivity. For the thermal expansion, we chose a tolerance of ±15%, which we derived by comparing several literature values[42]. For the heat capacity, the measured values from the literature are in quite good agreement with the first principle studies[14] and therefore we decided to estimate a tolerance of only ±5%. Comparing the elastic properties of diamonds from several literature values[43] leads to an estimated tolerance of ±10%. In combination with the previously mentioned tolerances for the UV spot size, the pulse energy and the initial temperature, the combinations of each minimum and maximum value have been calculated in a parametric sweep to estimate the overall tolerance of the simulation as illustrated in Fig. 4a-b. In Fig. 4c-d also a simulation considering the mean values is shown for a simulation time span of 10 μs. It should be mentioned that since the considered tolerances are based on literature values and are not directly measured, the actual values for the diamond crystal used in the experiment could fall outside these tolerances. Nevertheless, as the considered tolerances have been generously chosen, we anticipate that deviations beyond the specified tolerances are quite unlikely.
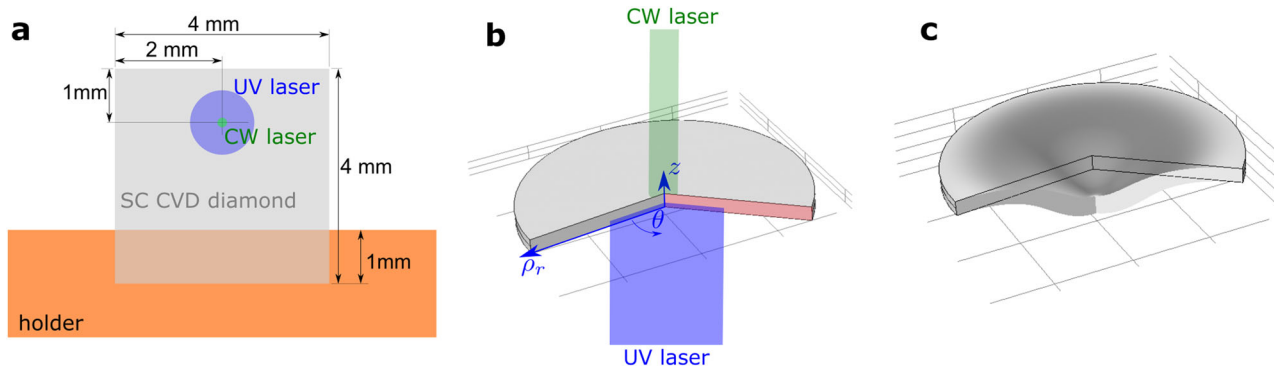
Fig. 2 | Visualization of aligned laser positions, crystal geometry, and heat load-induced deformation. a Aligned position of the UV laser and continuous wave (CW) laser on the single crystalline chemical vapor deposition (SC CVD) diamond. The area where the diamond crystal has contact with the holder is also illustrated here. The shape of the crystal considered in the simulation is shown in **b**. The sketch also illustrates the range where the UV laser is absorbed in the crystal. Further, the reflection of the CW laser at the surface relevant for our measurements is displayed. For visualization purposes, the transmission and successive reflection of the CW laser is not illustrated. This transmitted and successively reflected beam (at $z = 0$) returns, due to the wedge, under an angle with respect to the CW laser radiation reflected from the rear surface and thus is blocked by a pinhole as illustrated in Fig. 1a. The reflection of the CW laser at $z = 0$ is therefore not relevant for the interferometric measurement presented in this paper. The cutout of the actually cylindrical disk-like shape geometry in **b** and **c** is just used for exemplification of the interaction region and deformation shape, respectively. The red-marked surface in **b** is the only part of the three-dimensional structure that needs to be considered for the meshing due to the axisymmetry of the simulated case. In **c** a characteristic heat bump structure is shown, which can be observed when fixed boundary conditions at the lateral surface are considered. This static heat bump deformation can be observed for a temperature field induced by the energy distribution of the UV laser, when heat transfer is neglected. For better visibility, the deformation shown in **c**, which is actually in the nm range, has been scaled such that it is noticeable regarding the lateral crystal size, which is in the mm range.

The simulation calculates the complete deformation field which is induced by the UV laser inside the diamond crystal. Therefore, this simulation also provides the data of the displacement in z-direction (see the coordinate system in Fig. 2b) at the position where the CW laser is measuring. Since the CW laser has a finite beam radius the displacement data has to be weighted over the Gaussian beam shape profile. However, since the CW laser radius is significantly smaller than the UV laser radius the weighted value is almost the same as the displacement value directly in the center. Therefore, for the sake of reduced data amount the weighting has been neglected for the simulation data presented in Fig. 4.

Discussion
As mentioned before, the theoretical framework used for the simulation is based on the assumptions of a local thermodynamic equilibrium, classical mechanics and the empirical Fourier heat law. Further, the simulation considers an axisymmetric heat load profile and a cylindrical axisymmetric crystal geometry. It should be pointed out that it was not obvious that such a framework can predict the thermoelastic wave propagation, which has been measured in this work. Nevertheless, according to Fig. 4a, b, the simulation framework chosen in this work yields results which are, regarding the amplitude and signal shape, in good agreement with the interferometric measurements. However, some deviations in the measurement, especially at an initial temperature of 60 K, cannot be explained by the tolerances mentioned in the previous section. As it will be explained below, these deviations may be connected to a failure of the Fourier heat law. In the following section an interpretation of the measured signals in terms of the simulation results is also presented. These interpretations give a fundament of deeper understanding, which is helpful for the subsequent discussion regarding X-ray diffraction simulations. Following these interpretations, systematic errors will be discussed and the relevance of our findings for XFEL facilities with megahertz repetition rate will be emphasized.

Before directly interpreting the wave propagation, it is useful to consider related static deformations to understand important basic phenomena of the dynamic thermoelastic interaction. For the investigation of the static deformation of a crystal initially in thermodynamic equilibrium, heat transfer effects and transient changes of the displacement field have to be neglected. When such a system absorbs a single laser pulse this will cause static temperature gradients. Depending on the mechanical constrains and the shape of the heat load profile, these temperature gradients cause a characteristic deformation shape due to thermal expansion. The heat load considered in this work is connected to a Gaussian beam profile and an intensity exponentially decreasing in depth. This configuration results in a characteristic static heat bump deformation shape as illustrated in Fig. 2c. In general, due to the quantum solid-state effect of phonon-mode freezing and anharmonicity effects, the material parameters of the heat capacity and linear thermal expansion coefficients of a diamond crystal are significantly temperature dependent[38]. The quantum mechanical nature of these temperature dependencies makes their use in a transient simulation based on classical thermodynamics questionable. However, under the heuristic assumption, that a local thermodynamical equilibrium approximately exist it can be suspected, that the thermal stress, which is related to the ratio of the thermal expansion coefficient and the heat capacity, shows only a slight variation with temperature (<10%), in the range from 50 K to 350 K[14]. Following this argumentation, the shape and magnitude of the static heat bump structure is largely independent of the initial temperature of the diamond crystal, but is directly related to the energy density of the heat load profile.

After discussing a purely static case, the next step may be to consider a scenario where heat transfer is still being neglected, but the transient changes in the displacement field induced by absorption of a short laser pulse are taken into account. The rapid change of the temperature profile caused by the absorption of a laser pulse takes place on very short time scales (as mentioned before, thermalization takes place on the picosecond time scale). The rapid thermal expansion caused by this heat load will cause the well-known longitudinal wave propagation[31–33] and further the development of a heat bump[14]. Considering the dimensions of the crystal and heat load profile, our simulation result revealed that the time for the heat bump structure to fully develop is on the order of a few hundreds of ns. Further, the development of this heat bump structure is superimposed with a displacement field of propagating waves with magnitudes equal to the range of the static heat bump structure. Since heat transfer is neglected also in this case the thermal stress is almost directly connected to the energy density of the heat load profile and the propagating wave patterns are nearly independent of the initial temperature of the diamond crystal.

Finally considering now a case that includes conductive heat transfer, a significant dependence of the initial temperature can be observed for our
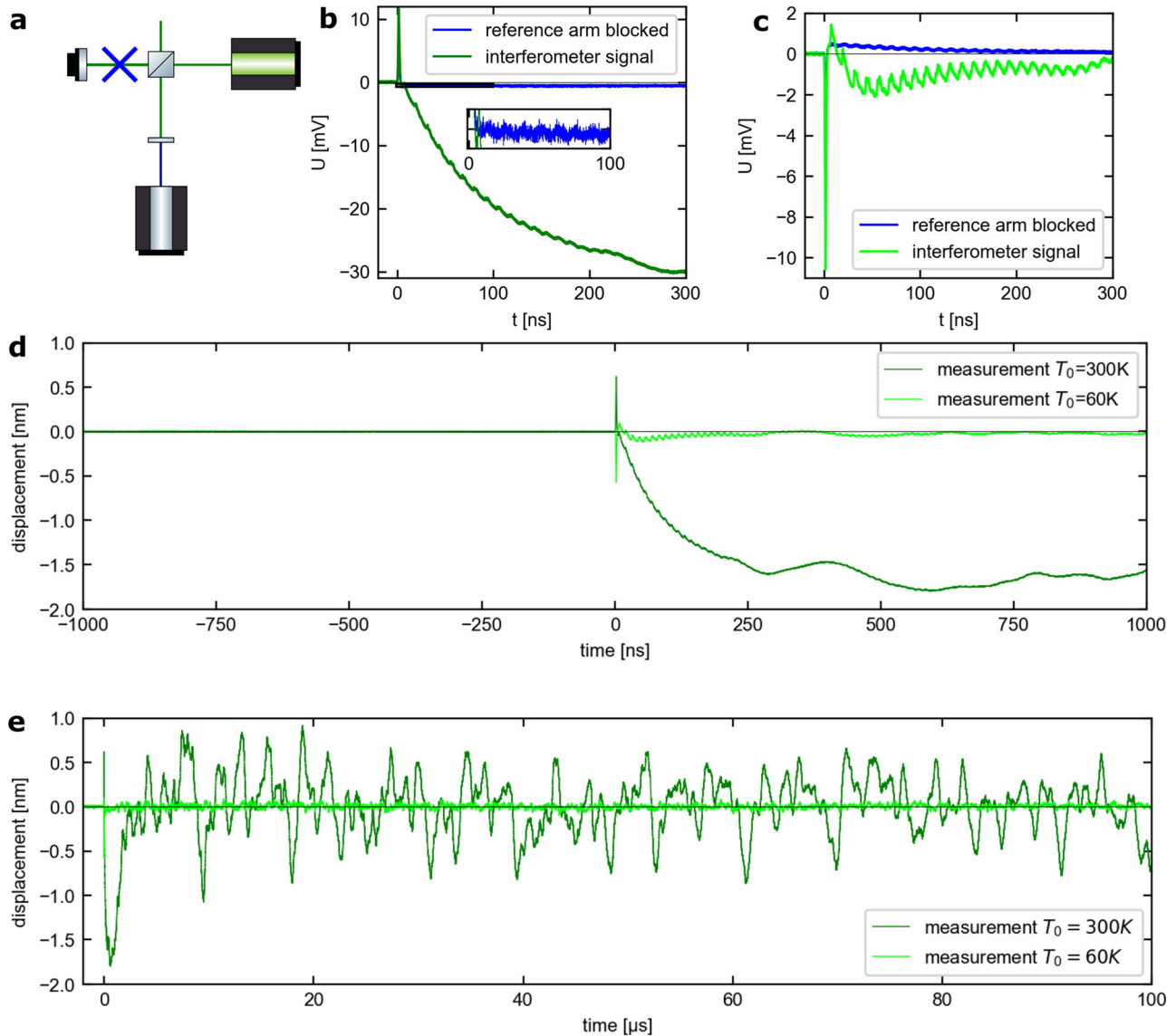
Fig. 3 | Analysis of systematic errors in interferometric measurements and assessing photon-matter interaction effects on displacement signals over time. a Simplified sketch of Fig. 1a. The blue cross marks the beam path which is blocked for a reference measurement to determine the signal contributions, which are not directly connected to a path length change of the interferometer arms. If the beam path is blocked at the marked position the experimental setup still measures a voltage signal with the oscilloscope. This signal is connected to a photon-matter-interaction-induced change of the refractive index. The change of the refractive index causes a systematic error in the determination of the displacement from the interferometer measurement. In **b** and **c**, a comparison of both signals indicates that the interferometric measurement is, apart from the strong initial peak, which occurs at the beginning of the photon-matter interaction near $t = 0$, the dominant signal. However, since the maximum reached displacement amplitude for an initial temperature of 300 K in **b** is significantly higher than for an initial temperature of 60 K in **c**, the systematic error has more noticeable relative impact on the low-temperature measurement. In **d** the measured displacement signals for the first 1000 ns after the photon-matter interaction are shown. Before the interaction (time < 0) the displacement is almost zero. In **e** the measured signal for a time span of 100 µs is shown. This is the maximum time span, which can be investigated with the experimental setup presented in this work. For the measurements at 300 K an average of over 2000 sweeps was done and for 60 K it was averaged over 10000 sweeps.

experimental configuration. The reason is the strong temperature dependence of the diffusivity. The diffusivity determines how fast a spatial temperature gradient can be changed in a finite time span. The heat bump structure development is caused by thermal stress resulting from the presence of a temperature profile with a significant temperature gradient. Hence, the diffusion process, which causes a decrease of the temperature gradient towards a homogeneous equilibrium temperature value, can have a strong impact on the development of the heat bump structure. Due to the high diffusivity of the diamond, the decay of the temperature gradient takes place on the same nanosecond time scale as relevant for the development of the heat bump. Therefore, the development of the heat bump amplitude is significantly reduced compared to a case where heat conduction is

neglected. Due to the temperature dependence of the material parameters the diffusivity of diamond is strongly dependent on the initial temperature. The much higher diffusivity of diamond at 60 K, being four orders of magnitude larger than at an initial temperature of 300 K, is the reason why the observed maximum amplitude in Figs. 3 and 4 is much lower at the lower initial temperature.

As mentioned before, the development of the heat bump structure is accompanied by wave propagation. Since the heat load profile has its maximum at the lateral center position of the crystal, a characteristic radial wave can be observed, which is initiated at this center position of the crystal and propagates towards the lateral boundaries. For the first 300 ns illustrated in Fig. 4a, b, reflections of radial waves at lateral boundaries do not
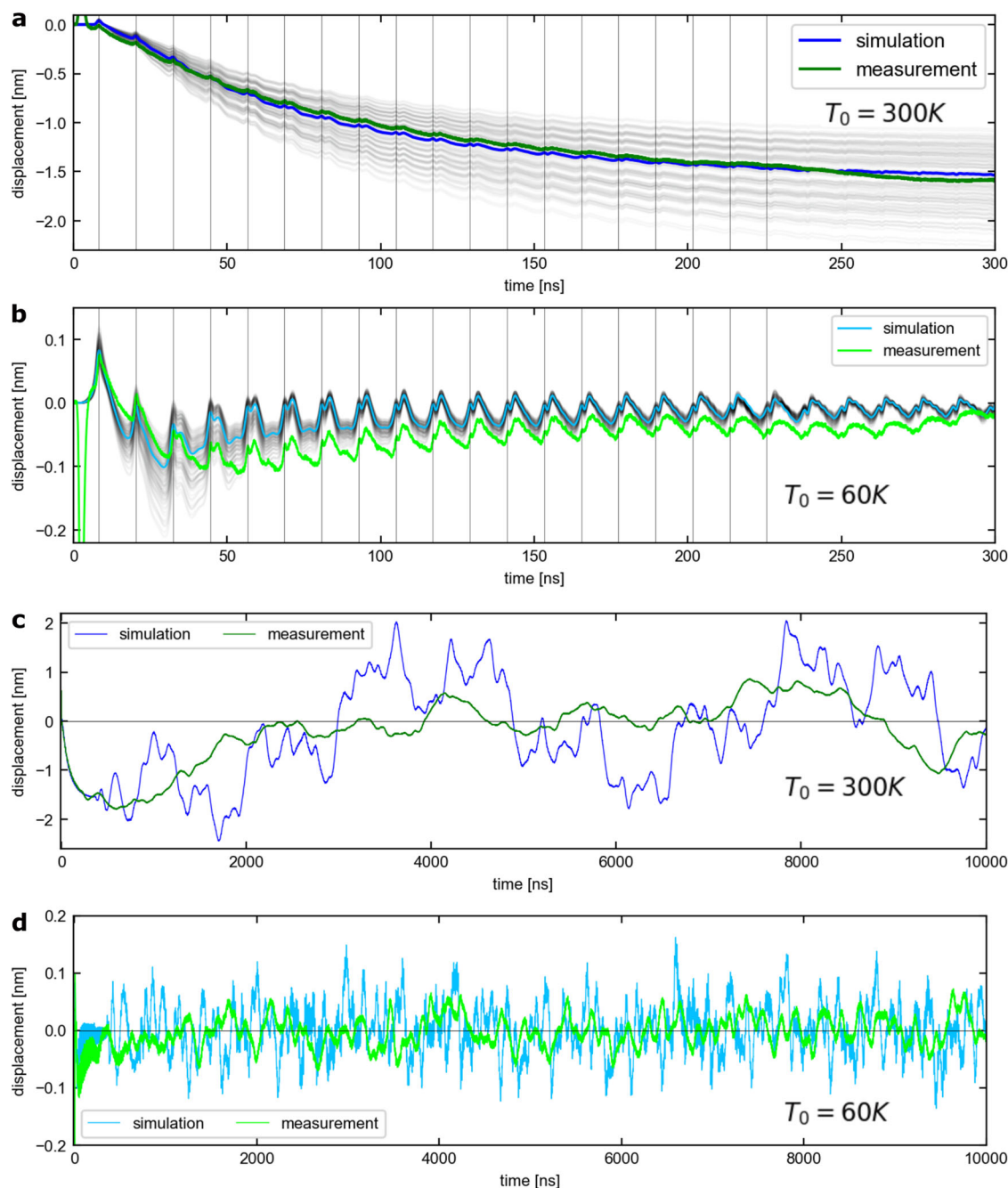
Fig. 4 | Comparative analysis between simulation and measurement results, considering initial temperatures and tolerance values in thermoelastic modeling. In **a** and **b** all combinations of the minimum and maximum tolerance values of seven different input parameters have been considered, resulting in 2^7 different curves which are illustrated in light gray color. A more precise error representation would be given if also the mean values would be considered, however this would have given 3^7 different curves. Such a calculation was avoided to shorten the computation time. The light gray curves can therefore be considered as a worst-case error estimate for the thermoelastic simulation. In addition to the gray lines also a blue solid line indicates the simulation results, obtained by using only the mean values for the input parameters. In **c** and **d** simulations are presented which only use the mean values of the input parameters, considering a time scale of 10 μs. In **a** and **c** an initial temperature of 300 K is considered. In **b** and **d** the initial temperature is 60 K. Deviations between simulations and measurement for time spans larger than 300 ns in **c** and **d** can be attributed to the different geometry considered in simulation versus measurement.

significantly influence the displacement development. However, for time spans greater than 300 ns the reflections at the lateral boundaries have a significant impact on the development of the measured displacement. The deviation observable in Fig. 4, d therefore most likely originates from the geometry and boundary conditions chosen for the simulation, where an axisymmetric geometry was considered instead of the cuboid-like structure (Fig. 2a).

To assess the influence of the thermoelastic strain on the X-ray reflection conditions, we exemplarily investigated the reflection conditions for a diamond crystal in 337 orientation, calculated by considering a two-beam case in symmetric geometry for a strained layer near back diffraction condition[15]. The choice of the 337 reflection is motivated by its potential application for a CBXFEL[24]. The timescale where an XFEL pulses interacts with the crystal is in the range of tens of fs and therefore the strain profile observed in an arbitrary timestep of the simulation can be directly used to calculate the reflection conditions. In Fig. 5a the reflection of an undisturbed crystal is illustrated. Considering our thermoelastic simulation, the mean amplitude of the strain value does not change significantly after the startup
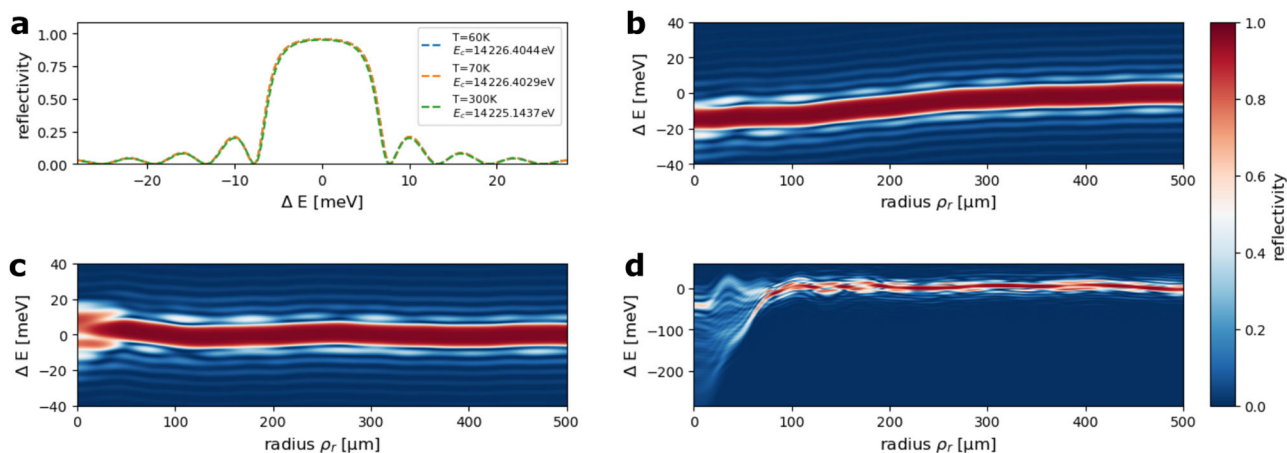
Fig. 5 | Reflection conditions simulation for backscattering in a 100 µm thick diamond crystal (337 Orientation) under thermoelastic induced strain variations. Simulation of reflection conditions for backscattering case of a 100 µm thick diamond crystal in 337 orientation. The energy deviation ΔE from the central energy E_c with reference to an initial crystal temperature is illustrated. **a** Reflection conditions for an unstrained crystal. Comparing the undisturbed curves, it can be seen that the undisturbed reflection curve shape is nearly independent of the temperature, but the central position significantly depends on the initial temperature, considering deviations in the meV range, as illustrated in the legend. **b–d** Reflection conditions of a strained crystal as a function of the radial coordinate ρ_r (as defined in Fig. 2b) calculated by considering axis symmetric thermoelastic simulation. Taking into account the strain given by thermoelastic effects shows deviation of the initial reflection conditions. **b** Initial temperature = 300 K, considered strain at t = 3µs after photon-matter interaction (**c**) Initial temperature = 60 K, considered strain at t = 3µs after photon-matter interaction. **d** Simulation results for the investigated case in our previous publication[14] at t = 222 ns, with an initial temperature of 70 K for a diamond Bragg reflector.

time of a few hundred of nanoseconds where rapid temperature change takes place due do diffusion. Therefore in Fig.5b, c, we can choose an arbitrary point in time after the startup, to get a representative distortion of the reflection condition. Interestingly, the thermoelastic strain component is in both cases on a similar level, however for the initial temperature of 300 K the thermoelastic deformations are superimposed with a quasi-static strain resulting from the remaining temperature difference with reference to the initial temperature, whereas for the 60 K the temperature value is sufficiently near an equilibrium value such that quasi-static strain effects are on a negligible level. These findings may sound surprising since one may intuitively expect a higher thermoelastic strain value for the 300 K case where the measured surface displacement is much higher (see Fig. 3). Nevertheless, the thermoelastic strain for 300 K is on a similar level since the displacement in the interaction region predominantly has a translational component which does not affect the reflection curve. Overall the distortion due to thermoelastic effects has a noticeable contribution, but the reflection curve is still near the undisturbed shape. In our previous work,[14] we investigated the thermoelastic effect for a simulated energy distribution of a CBXFEL[24], using the simulated strain value indicating much larger effects on the distortions of the reflection curve as illustrated in Fig. 5d. The reason for this can be referred to the difference in the beam radius and the effective penetration depth for the heat load profile and to the temporal shape of the UV laser pulse, which has with about 1 ns a longer pulse duration than the 600 ps considered in our previous work[14]. In general, not only the absorbed pulse energy, but also the spatial and temporal shape of the heat load profile can have a significant impact on thermoelastic effects. For example, a smaller beam radius, connected to focusing would increase the local energy density and can therefore aggravate thermoelastic effects. Also, due to thermoelastic effects the complex-valued reflectivity can vary strongly with transverse position on the crystal. Hence, an incoming wave reflected at the crystal will not only experience variations in the intensity, but also spatially dependent variation of the electric field, and, thus distortion of the wavefront[44].

To further assess the reliability of the findings, we will examine the impact of systematic errors in the upcoming discussion. A significant geometrical difference between the simulations and the measurement is that due to axisymmetric restrictions, the wedge of the diamond crystal could not be considered. Instead, a rectangular cross-section is used for the simulation. However, the systematic error given by this wedge angle may also be estimated with an axisymmetric simulation. In Fig. 4b it can be seen around 70 ns that, including all simulated tolerances, a deviation of about 30 pm between the measured signal and simulation is observed. Our simulations revealed that choosing a crystal radius of only 1 mm instead of 2 mm has no impact on the illustrated displacement shown in Fig. 4b, considering simulation time less than 80 ns. The wedge angle is about 0.1° which gives a thickness variation of 3.5 µm over a crystal diameter of 2 mm. Carrying out a simulation with thickness errors of 3.5 µm indicates that the difference in displacement is in the range of about 1.5 pm. Following this estimation, it can be concluded that the systematic error given by the wedge has only a minor effect on the signal and cannot explain the deviation between simulated and measured displacement.

As mentioned before, the signal change induced by the photon-matter interaction, illustrated in Fig. 3b, c, causes a signal which can be referred to a transient change of the refractive index. Comparison with our simulation data indicates that the transient change of the measured signal cannot simply be derived from the parameters of the displacement/strain and temperature. However, the oscillations observed in Fig. 3b, c show the same periodicity as observed for the interferometric signal, so that at least this effect can be linked to the longitudinal wave propagation[31–33]. The strong initial peaks and subsequent overshoot present in the beginning of the measurement is a surprising finding. At the measured position, the thermoelastically induced effects considered in our simulation predict that the temperature rise as well as the displacement should be almost zero at the moment of the photon-matter interaction. Hence, this strong initial peak cannot be explained with our theoretical framework. Considering the overshoot signal in Fig. 3c it can be observed that it causes an increase in intensity and therefore the before-mentioned deviation between the measured signal and simulation maybe even a few pm larger than indicated by the comparison in Fig. 4b. Unfortunately, the origin of the strong peak and overshoot could not be identified in our current investigation. It may be connected to free charge carrier dynamics[45], but a detailed investigation of this extensive topic is beyond the scope to this paper.

Even if not the complete time span covered by the measurement shown in Fig. 3e has been simulated, the simulation in Fig. 4 gives insights to the interpretation of rather long time scales. It can be seen in Fig. 4c-d that the maximum amplitude is reached in the very beginning of the measured time span. This initial time span can be connected to the time when the heat

bump structure builds up. After a time span of some hundreds of ns, the diffusion process leads to an almost constant temperature value at the thermal equilibrium, where almost no significant thermal stress is present afterwards. However, the waves, which have been created due to the rapid change of the temperature profile are still propagating and reflecting inside the crystal. The measurements in Fig. 3e reveal that the damping towards a negligible amplitude of these waves takes much longer than 100µs. The period of photon pulses at XFEL facilities with megahertz repetition is smaller than 1µs. Considering Fig. 3e, it is obvious that the amplitude of the displacement waves cannot be expected to be damped on the µs time scale. Therefore, displacement waves created by successive absorption of photon pulses will interact and their amplitudes possibly add up. The worst case would then be the resonant excitation of an eigenmode of the clamped crystal.

It should be mentioned that damping effects have not been considered in the context of this work. Single crystal diamond is known to have very low dissipation and is, therefore, a good choice for nanomechanical resonators with high-quality factors[46]. Unfortunately, for a stable Bragg reflector, a fast decay of elastic wave would be desired. There are several damping effects[47] which could be engineered to enhance the damping conditions. Therefore, investigating the possibility of a Bragg reflector with enhanced damping response may be another interesting topic for upcoming projects.

In addition to the optimization of damping effects, a promising approach for avoiding stability problems for Bragg reflectors under megahertz heat load may be using larger crystal structures. For thicker and lateral wider crystal structures the wave energy could be distributed over a larger volume. The amplitude of the reflected waves may be insignificant in the case of larger crystal structures.

Finally, for the simulations presented in this work, the Fourier heat law is used for modelling the heat diffusion process. However, as mentioned before, the underlying assumptions of the Fourier heat law may not be valid, owing to the lack of a local thermodynamical equilibrium at low temperatures. The discrepancy between the simulation and measurement in Fig. 4b may result from a failure of the Fourier heat law and an actually lower effective thermal conductivity[48] compared to the one used in the simulation. The conductivity value is directly proportional to the diffusivity. Therefore, a lower diffusivity could cause an increase of the heat bump amplitude and consequently, the deviation observed in Fig. 4b. However, describing non-Fourier phonon heat conduction[49] is a quite complex topic and is still an active field of research. Due to the complexity, the implementation of such a theoretical concept is beyond the scope of this paper. However, our measurements show that also outside the classical regime of thermodynamic equilibrium, thermoelastic excitations are clearly visible and do, at least approximately, follow the classical predications.

The findings presented in this paper reveal the stringed necessity for detailed investigations of dynamical thermoelastic effects for certain X-ray optics at XFEL facilities with megahertz repetition rate. Unlike the numerical and analytic approaches done in the literature, our measurements directly reveal the signature of these thermoelastic effects without relying on a number of partially strong assumptions. This is even more accentuated in the case of low crystal temperatures, where the assumption of thermodynamic equilibrium breaks down.

However, the axisymmetric simulation that we used seems to be a good starting point to simulate such effects. The good agreement between measurement and simulation in Fig. 4a, b indicates that our chosen theoretical framework gives reasonable predictions. We emphasize that our interferometer measurements only give information about the displacement at the surface of the crystal, the simulation however gives insights into the displacement field inside the crystal volume. The good agreement of the surface displacement in measurement and simulation is a strong indicator that also the volumetric displacement field has been predicted correctly by the simulation. The volumetric strain values as derived from the simulation may therefore be well applied to calculate the stability of a Bragg reflector using dynamical X-ray diffraction theory.

In conclusion, we present a direct measurement of three-dimensional dynamical thermoelastic effects in Bragg reflectors under characteristic heat load conditions for modern XFEL facilities, both at room temperature as well as cryogenic temperatures. With the presented theoretical framework, we have obtained simulation results with reasonable predictions for three-dimensional displacement wave propagation. At cryogenic temperatures, we observed deviations between simulation results and measurements at 60 K, which we connect to the failure of the Fourier heat law, indicating that the amplitude of the heat bump development is slightly underestimated by the simulations considering low initial temperatures. Nevertheless, also in this regime where the theoretical framework becomes questionable, the prediction of the three-dimensional wave propagation remains reasonable. Using the simulation framework presented in this paper, we already claimed in a recently published article that dynamical thermoelastic effects can heavily affect the performance of a CBXFEL[14], and the results we presented here prove that the applied theoretical framework is based on reasonable assumptions. In general, concerning the reflections conditions at Bragg reflectors for consecutive X-ray pulses, our findings can help in devising and interpreting all the applications at XFEL which experience powerful heat loads.[13,19–28]. However, three-dimensional numerical simulations of thermoelastic induced waves can be quite demanding in terms of computation time and further experimental data is desired to find appropriate ways of and reasonable approximations for modeling advanced topics like damping of displacement waves. Therefore, as a future perspective combining X-ray diffraction measurements and optical methods like interferometry as present in this work or knife-edge methods[50], is a promising attempt to assess the stability for Bragg reflectors and may open the pathway for the development of new X-ray optics optimized for powerful dynamical heat load.

Methods
Experimental setup
Most optical components of the experimental setup in Fig. 1a are placed on an optical table. However, the diamond crystal and the UV laser are placed beside the optical table. The diamond crystal is placed in a vacuum chamber with pressure $<10^{-6}$ mbar. The complete vacuum chamber, including the cryogenic cooler (TransMIT, PTS 8030-HT) can be aligned with motorized stages in all translational and rotational degrees of freedom. The alignment stages are mounted on top of a large granite block. The rotational stages are placed on top of the translational stage. On top of the translational stage also a support system for the UV laser is placed such that the UV laser can be aligned by translation motions against the crystal position.

For the Michelson interferometer, a linearly polarized continuous wave laser (COHERENT, Sapphire SF) with an output power of 150 mW is used. Polarizing beam splitter and half-wave retarders are used to guarantee that the reflected power from both interferometer arms have almost the same values. The quarter wave retarders are adjusted such that the beam propagation after reflection back into the laser housing is prevented. The beams coming from separate interference arms are aligned to have almost perfect spatial overlap. Using almost the same path length and focusing lenses in both interferometer arms ensures that the spot sizes of both beams are almost equal. To enable interference measurements, a polarizing beam splitter and half-wave retarders are used to create a measurable interference signal with opposite response to path length changes as sketched in Fig. 1a. (green1 and red2). One signal path is used to detect path length changes by an ultrafast photodiode (Newport, 1591NF) in combination with a high-speed oscilloscope (Teledyne LeCroy, WaveMaster 8 Zi-B). The other path is used to build up a working point stabilization. Here, a fast photodiode (Thorlabs, DET10A/M) is connected to the input of an analog PID controller (Stanford Research Systems, SIM960). The output of the PID controller is connected to a piezo amplifier (Physik Instrumente, E-617.00F), which adjusts with a mirror, mounted on a piezo (Physik Instrumente, P-885.11) the path length difference between the interferometer arms.

A fine alignment of the beams is carried out such that the measured voltage signal of the oscilloscope can reach a signal between a maximum value, for constructive interference, and an almost zero value, for destructive

interference. Variations between the maximum and minimum are randomly present on the time scales of a few ms if the working point stabilization is not activated. With the knowledge of the measured voltage signal values and the wavelength of the CW laser a conversion factor between displacement and voltage can be determined. For the calculation of this conversion factor, it is assumed that the path length change is mainly connected to a displacement of one of the interferometer arms.

Further information about the working principle of the interferometer, including the alignment procedure and information about additional models and manufacturers of the technical components can be found in a dissertation[37], which is related to this work.

UV laser
The optical UV laser (CryLas, FQSS 213-50), which we used for our pump-probe measurements has a wavelength of 213 nm, a pulse duration of about 1 ns, a pulse energy of (45 ± 5) μJ and a repetition rate of 20 Hz. The spatial and temporal function of the UV laser (CryLas, FQSS 213-50) has been measured with an ultrafast photodiode (ALPHALAS, UPD-200-UP) in combination with a high-speed oscilloscope (Teledyne LeCroy, Wave-Master 8 Zi-B). The measurement captured the rise and fall in reference to a nearly zero value. The normalization of the measured signal is performed, such that an integration over the rise and fall time yields unity. The normalized pulse shape data has been used for the numerical simulation to define the temporal shape of the heat load profile. The pulse energy was derived from an average power measurement with a thermal sensor and the manufacturer-specified repetition rate. The UV laser pulse temporal shape and amplitude is so stable that it can be assumed to be approximately constant for the needs of this paper.

Numerical simulation
The axisymmetric formulation of the thermoelastic equations and the heat source function considered in this work are nearly the same as presented in one of our preceded publications[14]. However, one difference in this paper is that we used the measured temporal pulse shape of the UV laser instead of a Gaussian function for the heat source function. The thermoelastic PDEs were solved with the software COMSOL Multiphysics® 6. The generalized alpha time solver was used with a constant time stepping of 50 ps. For the mesh quadratic shaped elements with length and width of 5 μm were used. However, at the top surface, a distributed mesh with reduced size in z-direction (z-direction as defined in Fig. 2b) is used to have a higher resolution in the range of the UV lasers penetration depth area. To take into account the temperature-dependent material parameters a Newton-Raphson method is used. Thermal insulating boundary conditions are considered for the entire domain. The mechanical boundary conditions are that the lateral sides have fixed constraints and the remaining surfaces are stress-free.

Material parameters for simulation
For the temperature-dependent material parameters the derived values of Jacobson and Stoupin (Fit1) for the thermal expansion coefficient[42] were used. For thermal conductivity, we used the values obtained by Wei et al.[41] for a crystal with 1.1% ^{13}C isotope content. For the heat capacity values calculated[37] by a first principle simulation were used. Further, the approximately temperature-independent material parameters for the Young's module with 1125 GPa, the Poisson's ratio with 0.076 and the mass density with 3516 kg/m³ were used. For the reflectance under normal incident and the penetration depth at the wavelength 213 nm of the UV laser the literature values 0.22128 and 5 μm, respectively, have been used. Preliminary measurements with our experimental setup investigating the transmitted UV laser pulse energy for a 100 μm thick high-temperature high-pressure diamond crystal revealed that the variation of the penetration depth is less than 30 nm in the investigated temperature range[37]. Therefore, it can be neglected in the context of this paper. It should be mentioned that for this measurement it was assumed that the change of the transmission is mainly connected to the change of the penetration depth. However, the change of the transmission could have also resulted from a change of the reflectivity. Unfortunately, measuring the reflected pulse energy was not possible with our current experimental setup.

Calculation of crystal thickness
The well-known longitudinal wave propagation[31–33,37] gives the possibility to calibrate the thickness of the diamond crystal for our simulation. The longitudinal speed of sound v_L may be calculated by $v_L = \sqrt{E(1-\nu)/(\rho(1+\nu)(1-2\nu))}$, where ρ is the mass density, E is the Young's module and ν the Poisson's ratio. The measured fringe periodicity T_p illustrated in Fig. 4a-b can then be used to calculate $d = T_p v_L/2$, where the d is the crystal thickness.

Diamond crystal
The diamond crystal was fabricated with microwave plasma CVD technique by Applied Diamond, Inc. The crystal has the nominal dimensions 4 mm × 4 mm × 100 μm. The orientation is <100>. The wedge angle is about 0.1°, which corresponds to a thickness variation of about $\tan(0.1°) \times 4$ mm = 7 μm. The manufacturer information is that the ^{13}C content of the diamond crystal is about 1.1%.

Measurement of the laser spot size
The shape of the CW laser beams has been measured with a beam profiler revealing an almost perfectly Gaussian shape, measured at several positions in the experimental setup. However, beam profile measurements of the UV laser, with a beam profiler (Newport, LBP2-HR-VIS) in combination with a UV converter (DataRay Inc., BSF08R12N), indicated some variations in the diameter[37]. To determine the spot size at the position of the diamond crystal a knife edge technique[39] was used. For the UV laser, the diamond crystal itself has been used as a knife edge. However, due to the transparency at the wavelength of the CW laser, using directly the diamond crystal was not applicable. Therefore, it was replaced by a 100 μm thick silicon crystal for the knife edge measurement. Combining the result of the beam profile measurement and the spot size value obtained by the knife edge measurement we concluded that a reasonable approximation for the UV laser beam at the position of the crystal is a Gaussian profile with a beam radius of (300.7 ± 12) μm. The variation of the spot size of the CW laser is expected to be neglectable for the needs of this work, since it only has an impact on the weighted average value of the displacement measurement, but is not relevant for the input parameters of the thermoelastic simulation.

Data availability
The data that support the plots within this paper and other findings of this study are available from the corresponding author upon reasonable request.

Code availability
The COMSOL Multiphysics® files used to generate the simulation are available upon request.

References
1. Decking, W. et al. A MHz-repetition-rate hard X-ray free-electron laser driven by a superconducting linear accelerator. *Nat. Photonics* **14**, 391–397 (2020).
2. Schoenlein, R. W., Boutet, S., Minitti, M. P. & Dunne, A. M. The linac coherent light source: recent developments and future plans. *Appl. Sci.* **7**, 850 (2017).
3. Huang, N., Deng, H., Liu, B., Wang, D. & Zhao, Z. Features and futures of X-ray free-electron lasers. *Innovation* **2**, 100097 (2021).
4. Sobolev, E. et al. Megahertz single-particle imaging at the European XFEL. *Commun. Phys.* **3**, 1–11 (2020).
5. Gisriel, C. et al. A Membrane protein megahertz crystallography at the European XFEL. *Nat. Commun.* **10**, 1–11 (2019).

6. Pandey, S. et al. Time-resolved serial femtosecond crystallography at the European XFEL. *Nat. Methods* **17**, 73–78 (2020).

7. Boll, R. et al. X-ray multiphoton-induced Coulomb explosion images complex single molecules. *Nat. Phys.* **18**, 423–428 (2022).

8. Grünbein, M. L. et al. Effect of X-ray free-electron laser-induced shockwaves on haemoglobin microcrystals delivered in a liquid jet. *Nat. Commun.* **12**, 1–11 (2021).

9. Bushuev, V. Effect of the thermal heating of a crystal on the diffraction of pulses of a free electron x-ray laser. *Bull. Russ. Acad. Sci.: Phys.* **77**, 01 (2013).

10. Qu, Z., Ma, Y., Zhou, G. & Wu, J. Analytical model for monochromator performance characterizations under thermal load. *Opt. Express* **28**, 30075–30084 (2020).

11. Yang, C. et al. X-ray diffraction performance of thermally distorted crystals. *High. Power Laser Sci. Eng.* **11**, e69 (2023).

12. Petrov, I. et al. Performance of a cryo-cooled crystal monochromator illuminated by hard X-rays with MHz repetition rate at the European X-ray Free-Electron Laser. *Opt. Express* **30**, 4978–4987 (2022).

13. Liu, S. et al. Cascaded hard X-ray self-seeded free-electron laser at megahertz repetition rate. *Nat. Photonics* **17**, 984–991 (2023).

14. Bahns, I., Rauer, P., Rossbach, J. & Sinn, H. Stability of Bragg reflectors under megahertz heat load at XFELs. *J. Synchrotron. Radiat.* **30**, 1–10 (2023).

15. Kohn, V. G. A theory of multiple Bragg diffraction of x-rays in multilayer crystal systems. *J. Mosc. Phys. Soc.* **1**, 425–434 (1991).

16. Gronkowski, J. Propagation of x-rays in distorted crystals under dynamical diffraction. *Phys. Rep.* **206**, 1–41 (1991).

17. Honkanen, A. P., Ferrero, C., Guigay, J. P. & Mocella, V. A finite-element approach to dynamical diffraction problems in reflection geometry. *J. Appl. Crystallogr.* **51**, 514–525 (2018).

18. Krzywinski, J., & Halavanau, A. Time-dependent dynamical Bragg diffraction in deformed crystals by the beam propagation method. *Acta Crystallogr. A: Found. Adv.* **78**, 465–472 (2022).

19. Kujala, N. et al. Hard x-ray single-shot spectrometer at the European X-ray Free-Electron Laser. *Rev. Sci. Instrum.* **91**, 103101 (2020).

20. Samoylova, L. et al. Diffraction properties of a strongly bent diamond crystal used as a dispersive spectrometer for XFEL pulses. *J. Synchrotron. Radiat.* **26**, 1069–1072 (2019).

21. Rich, D. et al. The LCLS variable-energy hard X-ray single-shot spectrometer. *J. Synchrotron. Radiat.* **23**, 3–9 (2016).

22. Liu, S. et al. Preparing for high-repetition-rate hard x-ray self-seeding at the European X-ray Free Electron Laser: Challenges and opportunities. *Phys. Rev. Accel. Beams* **22**, 060704 (2019).

23. Rauer, P. et al. Cavity based x-ray free electron laser demonstrator at the European X-ray Free Electron Laser facility. *Phys. Rev. Accel. Beams* **26**, 020701 (2023).

24. Huang, N. & Deng, H. Thermal loading on crystals in an X-ray free-electron laser oscillator. *Phys. Rev. Accel. Beams* **23**, 090704 (2020).

25. Kim, K. J. & Shvyd'ko, Y. V. Tunable optical cavity for an x-ray free-electron-laser oscillator. *Phys. Rev. Spec. Top.-Accel. Beams* **12**, 030703 (2009).

26. Freund, H. P., Van der Slot, P. J. M. & Shvyd'ko, Y. An X-ray regenerative amplifier free-electron laser using diamond pinhole mirrors. *N. J. Phys.* **21**, 093028 (2019).

27. Marcus, G. et al. Refractive guide switching a regenerative amplifier free-electron laser for high peak and average power hard x-rays. *Phys. Rev. Lett.* **125**, 254801 (2020).

28. Halavanau, A. et al. Population inversion X-ray laser oscillator. *Proc. Natl Acad. Sci.* **117**, 15511–15516 (2020).

29. Shvyd'ko, Y., Blank, V. & Terentyev, S. Diamond x-ray optics: Transparent, resilient, high-resolution, and wavefront preserving. *MRS Bull.* **42**, 437–444 (2017).

30. Ziaja, B., Medvedev, N., Tkachenko, V., Maltezopoulos, T. & Wurth, W. Time-resolved observation of band-gap shrinking and electron-lattice thermalization within X-ray excited gallium arsenide. *Sci. Rep.* **5**, 1–7 (2015).

31. Thomsen, C., Grahn, H. T., Maris, H. J. & Tauc, J. Surface generation and detection of phonons by picosecond light pulses. *Phys. Rev. B* **34**, 4129 (1986).

32. Rose-Petruck, C. et al. Picosecond–milliångström lattice dynamics measured by ultrafast X-ray diffraction. *Nature* **398**, 310–312 (1999).

33. Stoupin, S. et al. Direct observation of dynamics of thermal expansion using pump-probe high-energy-resolution x-ray diffraction. *Phys. Rev. B* **86**, 054301 (2012).

34. Nowacki, W. Thermoelasticity. (Elsevier, 2013).

35. Yang, B., Wang, S. & Wu, J. Transient thermal stress wave and vibrational analyses of a thin diamond crystal for X-ray free-electron lasers under high-repetition-rate operation. *J. Synchrotron Radiat.* **25**, 166–176 (2018).

36. Qu, Z. Photo-thermo-mechanical analysis and control for high-brightness and high-repetition-rate x-ray optics. (University of California, Merced, 2020).

37. Bahns, I. Nondestructive interaction of powerful electromagnetic waves with Bragg reflectors. (Doctoral dissertation, Staats-und Universitätsbibliothek Hamburg Carl von Ossietzky, 2021).

38. Gross, R., Marx, A., Einzel, D., & Geprägs, S. Festkörperphysik. (De Gruyter., 2018).

39. de Araújo, M. A., Silva, R., de Lima, E., Pereira, D. P. & de Oliveira, P. C. (2009). Measurement of Gaussian laser beam radius using the knife-edge technique: improvement on data analysis. *Appl. Opt.* **48**, 393–396 (2009).

40. Phillip, H. R. & Taft, E. A. Kramers-Kronig analysis of reflectance data for diamond. *Phys. Rev.* **136**, A1445 (1964).

41. Wei, L., Kuo, P. K., Thomas, R. L., Anthony, T. R. & Banholzer, W. F. Thermal conductivity of isotopically modified single crystal diamond. *Phys. Rev. Lett.* **70**, 3764 (1993).

42. Jacobson, P. & Stoupin, S. Thermal expansion coefficient of diamond in a wide temperature range. *Diam. Relat. Mater.* **97**, 107469 (2019).

43. Hess, P. The mechanical properties of various chemical vapor deposition diamond structures compared to the ideal single crystal. *J. Appl. Phys.* **111**, 3 (2012).

44. Rauer, P. A Proof-Of-Principle Cavity-Based X-Ray Free-Electron-Laser Demonstrator at the European XFEL (Doctoral dissertation, Deutsches Elektronen-Synchrotron DESY, 2022).

45. Ivakin, E. V. E. et al. Investigation of free charge carrier dynamics in single-crystalline CVD diamond by two-photon absorption. *Quantum Electron.* **44**, 1055 (2014).

46. Tao, Y., Boss, J. M., Moores, B. A. & Degen, C. L. Single-crystal diamond nanomechanical resonators with quality factors exceeding one million. *Nat. Commun.* **5**, 1–8 (2014).

47. Rodriguez, J. et al. Direct detection of Akhiezer damping in a silicon MEMS resonator. *Sci. Rep.* **9**, 1–10 (2019).

48. Qu, Z., Ma, Y., Zhou, G. & Wu, J. Numerical characterization of quasi-steady thermal load for thin crystal at cryogenic temperature with nondiffusive heat transfer. *J. Appl. Phys.* **130**, 144503 (2021).

49. Chen, G. Non-Fourier phonon heat conduction at the microscale and nanoscale. *Nat. Rev. Phys.* **3**, 555–569 (2021).

50. Monchalin, J.-P. Optical Detection of Ultrasound. *IEEE Trans. Ultrason. Ferroelectr. Freq. Control* **33**, 485–499 (1986).

Acknowledgements

Author contributions

I.B. built up the experiential setup, carried out the thermoelastic simulations, as well as, the measurements and conceived the experiment. P.R. contributed in the development of the theoretical framework and carried out

the dynamical X-ray diffraction simulations. S.S. proposed the optical design for the interferometer. J.R. initiated the experimental project and, with H.S. supervised and contributed with regular discussions to the project. The first draft of the manuscript was written by I.B., afterwards all the authors discussed the results and contributed to writing the manuscript.

Competing interests
The authors declare no competing interests.

Additional information
Supplementary information The online version contains supplementary material available at https://doi.org/10.1038/s42005-024-01581-1.

Correspondence and requests for materials should be addressed to Immo Bahns.

Peer review information *Communications Physics* thanks Kwang-Je Kim and the other, anonymous, reviewer(s) for their contribution to the peer review of this work. A peer review file is available.

Reprints and permissions information is available at http://www.nature.com/reprints

Publisher's note Springer Nature remains neutral with regard to jurisdictional claims in published maps and institutional affiliations.